Mechanics of Advanced Materials and Structures

ISSN: (Print) (Online) Journal homepage: www.tandfonline.com/journals/umcm20

Mechanical behavior of friction stir butt welded joints under different loading and temperature conditions

Lucas Pinto, Gonçalo Cipriano, Daniel F. O. Braga, Catarina Vidal, Miguel A. Machado, Arménio Correia & Virgínia Infante

To cite this article: Lucas Pinto, Gonçalo Cipriano, Daniel F. O. Braga, Catarina Vidal, Miguel A. Machado, Arménio Correia & Virgínia Infante (2024) Mechanical behavior of friction stir butt welded joints under different loading and temperature conditions, Mechanics of Advanced Materials and Structures, 31:7, 1413-1422, DOI: 10.1080/15376494.2022.2137886

To link to this article: https://doi.org/10.1080/15376494.2022.2137886

MECHANICS OF ADVANCED MATERIALS AND STRUCTURES
2024, VOL. 31, NO. 7, 1413–1422
https://doi.org/10.1080/15376494.2022.2137886

Taylor & Francis
Taylor & Francis Group

ORIGINAL ARTICLE

Mechanical behavior of friction stir butt welded joints under different loading and temperature conditions

Lucas Pinto[a], Gonçalo Cipriano[b], Daniel F. O. Braga[b], Catarina Vidal[c], Miguel A. Machado[c], Arménio Correia[d], and Virgínia Infante[d]

[a]Department of Mechanical Engineering, Instituto Superior Técnico, Universidade de Lisboa, Lisboa, Portugal; [b]Department of Mechanical Engineering, Institute of Mechanical Engineering and Industrial Management (INEGI), Porto, Portugal; [c]UNIDEMI, Department of Mechanical and Industrial Engineering, NOVA School of Science and Technology, Universidade Nova de Lisboa, Lisboa, Portugal; [d]Department of Mechanical Engineering, LAETA, IDMEC, Instituto Superior Técnico, Universidade de Lisboa, Lisboa, Portugal

ABSTRACT

Friction Stir Welding is a process that has led to increasing usage of aluminum and its alloys in different industries, since it is an autogenous and a solid-state welding process. The work developed in this paper was focused on the analysis of the mechanical behavior of AA7075-T651 friction stir butt welded joints, of 4 mm of thickness, under different loading and temperature conditions. A selection process was applied to assure the appropriate welding parameters. The welds from which the investigated specimens were manufactured from were submitted to nondestructive testing to assess the presence of welding defects. Fatigue tests were carried out, under a constant amplitude loading regime, at stress ratios of 0.05 and 0.5 and at temperatures of 23 °C and 150 °C. The results obtained by the fatigue tests point to a higher fatigue life of the specimens when the highest stress ratio, R = 0.5, was used (for the maximum stress applied), for both loading temperatures. For the stress range, the contrary was found to be true. Room temperature was also found to result in a significantly better fatigue performance. A Scanning Electron Microscope was used to characterize the fatigue fracture surfaces.

ARTICLE HISTORY
Received 23 May 2022
Accepted 16 October 2022

KEYWORDS
Friction Stir Welding; fatigue; stress ratio; temperature; AA7075-T651; welding defects

1. Introduction

Aluminum and its alloys have seen their application in multiple industries increase over the last years, as a result of the development of a joining process that enables the joining of such metallic alloys with excellent mechanical properties: Friction Stir Welding (FSW). FSW is a solid-state welding process during which melting of the base material does not occur. This allows aluminum alloys that were thought to be not weldable to be welded [1]. As for its working principles, a non-consumable, rotating, hardened steel tool, with a cylindrical shape constituted by a probe and a shoulder, is driven into the intended weld joint location until the probe has completely penetrated the material and the shoulder is in contact with the surface of the workpieces. The rotating speed of the tool generates heat (by interfacial and internal friction dissipation) and plastic strain that promote the weld of the workpieces. As the tool moves along the weld line (welding/travel speed), the material is stirred from the leading edge of the probe into its trailing edge, being thermo-mechanically processed, obtaining the desired weld by stirring/mixing the materials. Additionally, and since it is an autogenous welding process, no filler material is required to achieve the joining of the materials, hence allowing designs composed by lighter structural components. The joints achieved with FSW have excellent structural integrity and reduced weld affected microstructure zone, even enabling dissimilar material joining [2]. These factors combined have made FSW a prime candidate for structural applications in automotive, aeronautical and aerospace applications. As such, FSW has generated significant research and development effort to mature the technology, enable more applications and increase the technical and economic viability of the process. One more recent development is high-speed FSW, enabling high volume EV battery pack production with weld speeds up to 4.5 m/min [3, 4]. One important area of development in the field of FSW has been tools capable of optimizing process heat input, enabling more material combinations, higher performing joints, or higher speed welds. Tools such as Bobbin Tool and Stationary Shoulder Tool, lead to derivatives of FSW, such as Bobbin Tool FSW (BTFSW) and Stationary Shoulder (SSFSW). Sejani et al. [5] reviewed the recent developments in SSFSW and compared resulting joints and process with BTFSW, showing that SSFSW leads to finer more optimized microstructures. Besides tooling, process control has also been a point of focus of recent research, to enable and enhance self-supported FSW, non-weld-thinning FSW and frictional stir-based remanufacturing [6].

CONTACT Virgínia Infante virginia.infante@tecnico.ulisboa.pt Department of Mechanical Engineering, LAETA, IDMEC, Instituto Superior Técnico, Universidade de Lisboa, Lisboa, Portugal.

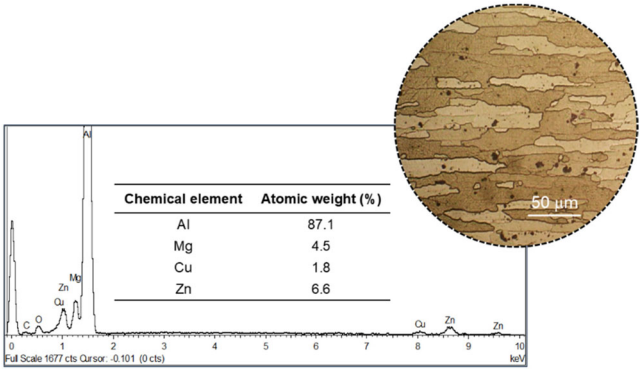

Figure 1. AA7075-T651 microstructure and chemical elemental composition determined by energy dispersive X-ray spectroscopy (EDS).

Just like any other welding process, FSW can produce defective joints, if the parameters are not appropriate. A common defect in aluminum FSW joints is the Kissing Bond Crack which are usually located in the weld root and results from a lack of mechanical and chemical bond between the original materials. These root defects exhibit a particular morphology which is characterized by considerable small size and no physical discontinuity. Nondestructive Techniques (NDT) such as Eddy Currents (EC) have demonstrated high reliability in the detection of said defects since the joint comprises electric conductive materials and these defects are usually close to the surface [7]. However, since the FSW process generates distinct microstructural regions with different grain morphologies, the electric conductivity changes along the weld, particularly considering the transversal direction to the weld bead. The EC technique can measure impedance changes caused by the presence of the defect, with the analysis of the results leading to the determination of the presence of set defects [8]. Microstructural modifications such as grain refinement and precipitation in AA7075 has been reported in the literature, leading to the distinct microstructural regions [9].

Since most of the structural components are subjected to dynamic loading conditions that may lead to the failure of the entire structure, fatigue behavior of friction stir welded joints became a prominent field of research. In fact, fracture induced by fatigue is the principal cause of failure in joints obtained by means of FSW [10]. The loading temperature and stress ratio (R) are some of the factors that influence the fatigue crack growth rate and consequently play an important role in their fatigue performance.

There are several researchers who have published in literature their works on studying and evaluating the effect of these parameters over the fatigue life of welds obtained by FSW. Some examples are presented next.

Resan et al. [11] found that the fatigue life of welds obtained by FSW decreased with an increase in the temperature at which the fatigue tests were being performed. The research consisted in the investigation of the effect of both the loading temperature and tool rotational speed over the fatigue life of AA2024 friction stir welds. It was concluded that for the same tool rotational speed, increasing the fatigue testing temperature had a detrimental effect over the fatigue life of the welds.

Table 1. AA7075-T651 mechanical properties [8].

Mechanical property	
Yield strength (YS)	503 MPa
Ultimate tensile strength (UTS)	572 MPa
Modulus of Elasticity	72 GPa
Vickers hardness	193 (HV2.0)

In another work, Tra et al. [12] witnessed that the fatigue crack growth rates were influenced by the temperature at which the fatigue tests were carried out. A comparison was made between the rates obtained at room temperature and at 200 °C. The results point out to the same conclusion as those obtained by Resan et al. [11]. These experiments were performed with AA6063-T5 FS welded joints.

Li [13] observed the effect of different stress ratios over the fatigue crack growth rate of AA7075-T651 friction stir welds. Li [13] was able to conclude that higher stress ratios have a more detrimental effect on the fatigue life of the welds since higher stress ratios led to higher fatigue crack growth rates. From the experimental work that was developed it was also possible to see that this effect becomes less significant as the stress ratio value increases.

No work regarding both, the effect of the loading temperature and stress ratio over the number of cycles until failure of this type of welds, was found in the available literature. Therefore, the present work was developed focusing on the analysis of the mechanical behavior of AA7075-T651 friction stir butt welded joints, of 4 mm of thickness, under different loading, $R = 0.05$ and $R = 0.5$, and temperature conditions, 23 °C and 150 °C.

2. Materials and methods

2.1. Base material characterization

The base material used consisted of AA7075 rolled plates with a thickness of 4 mm, in the T651 condition. Their elemental chemical composition was assessed by the corresponding X-ray energy dispersive spectrometer (EDS) as presented in Figure 1. Four alloying elements were identified: Aluminum (Al), Magnesium (Mg), Copper (Cu) and Zinc (Zn), with the main alloying element being Zinc, as expected, considering that it is an alloy from the 7XXX series [14]. A microstructural analysis of the unprocessed aluminum alloy was performed using an Olympus CK40M Compact Inverted Metallurgical Microscope equipped with an Olympus C3040-ADL Digital Camera. A sample was mounted in epoxy resin, grinded and polished following standard metallographic procedures and then etched in Keller's reagent (2.5 mL HNO3, 1.5 mL HCl, 1 mL HF and 95 mL H2O), for 10 s. In Table 1, some of the AA7075-T651 mechanical properties are listed.

2.2. Production of the friction stir welded joints

All the friction stir welded joints were produced on an ESAB LEGIOTM FSW 3UL® numeric control machine. The machine contains a welding head capable of moving along the X, Y and Z axis. A modular non-consumable tool made

Table 2. Range of the welding parameters used throughout the production of the welds.

Process parameter	Range of values
Welding position (prescribed)	[0.08, 0.8] mm
Tool vertical force	[4, 10] kN
Tool rotation speed	[800, 2000] rev/min
Tool plunge speed	[0.05, 0.1] mm/s
Dwell time	[3, 10] s
Welding speed	[40, 150] mm/min

of H13 steel comprised by a scrolled shoulder, with outer and inner diameters of 16 mm and 5 mm, respectively, and a conical lefthanded thread probe with a diameter of 5 mm and a length of 3.9 mm, rotated in the clockwise (CW) direction was used.

A selection process that allowed the determination of an appropriate set of welding parameters was carried out by performing a total of 23 trial tests, with the range of parameters listed in Table 2. The welds with no defects detectable by visual inspection were then subject to a more specific and precise nondestructive evaluation, as described in Section 2.3. Uniaxial quasi-static tension tests were carried out on the welds with no defects detectable by the Eddy current technique, in order to identify the welds with the highest mechanical performance. Finally, optical microscopy (MO) was used either to double check the presence of the defects identified or to confirm the absence of defects in the welds with the best mechanical properties. Based on these results, non-defective welds were produced using the parameters presented in Table 3 to produce specimens to carry out fatigue testing at two temperatures and stress ratios.

2.3. Eddy current testing

The welds were submitted to nondestructive tests to assess the existence of welding defects at the Nondestructive Testing Laboratory, located at the Nova School of Science and Technology. Eddy Current Testing (ECT) was used for this purpose as it has a very high sensitivity to surface and sub surface defects, as it the case of weld root defects, and applicable to electrically conductive materials such as the alloy welded in this study [15]. The experimental implementation was performed by means of an automated scanning device, an XYZ table, responsible for the probe movement while the sample remains stationary. The movement, as well as the signal acquisition, were controlled and programmed in LabVIEW environment. Regarding the equipment, an ECT absolute pencil probe with 2 mm diameter with a fixed air-loaded reference coil in bridge mode operating at 1.1 MHz, combined with an Olympus Nortec 600 D digital ECT instrument (to excite and acquire the probe signals), were used in the tests.

2.4. Macro and microstructural characterization of the welds

Macro and microstructural analyses of the welds were conducted using the procedure and optical microscope described in Section 2.1. All samples were produced using cross-sections from the welds, transverse to the welding direction. The welds subject to optical microscopy observations were either those with root defects detected by EC testing, as depicted in Figure 2, or that produced with the parameters indicated in Table 3. In addition to the welding defects, the main microstructural regions, namely the dynamic recrystallization zone (nugget), the thermo-mechanically affected zone (TMAZ) and the heat-affected zone (HAZ) were identified and characterized, as well.

Table 3. Welding parameters used to produce the welds.

Process parameter	
Welding position (prescribed)	0.8 mm
Tool vertical force	9.5 kN
Tool rotation speed	1000 rev/min
Tool plunge speed	0.1 mm/s
Dwell time	4 s
Welding speed	80 mm/min

2.5. Hardness measurements on the welds

The mechanical strength of a friction stir welded joint is a result of the thermal cycle and severe plastic deformation that the material undergoes during this solid-state welding process and, it can be qualitatively assessed through hardness measurements. Therefore, those were performed using a Mitutoyo AVK-C2 hardness tester on polished and etched cross-section samples of the welds, according to the ASTM E384 − 10 standard. For each weld, indentations were made along 3 different straight lines: at 0.5 mm from the top surface of the weld, at the mid-thickness of the weld and at 3.5 mm from the top surface of the weld, with a load of 2 kgf and an indentation time of 10 s. The spacing between consecutive indentions was 1 mm for the base material and 0.5 mm for processed and thermal/mechanical affected regions.

2.6. Uniaxial quasi-static testing

Preliminary uniaxial quasi-static tensile tests were performed at room temperature to assess the mechanical strength of the welds produced at the welding parameters determination stage. Based on these results, a set of welding parameters was established as listed in Table 3. The welds produced with this set of welding parameters were then subject to additional uniaxial quasi-static tensile tests at room (∼23 °C) and at elevated temperature (150 °C). The tensile specimens used were manufactured from the welded plates, transversally to the welding direction. Testing was carried out at a displacement rate of 5 mm/min following standard testing procedures. For the tests performed at 150 °C, an Instron furnace equipped with a temperature controller was used to control the testing temperature and to ensure that the tensile tests were performed, entirely, at the desired temperature. The testing equipment used for this purpose was an Instron 3369, with a load cell of 50 kN.

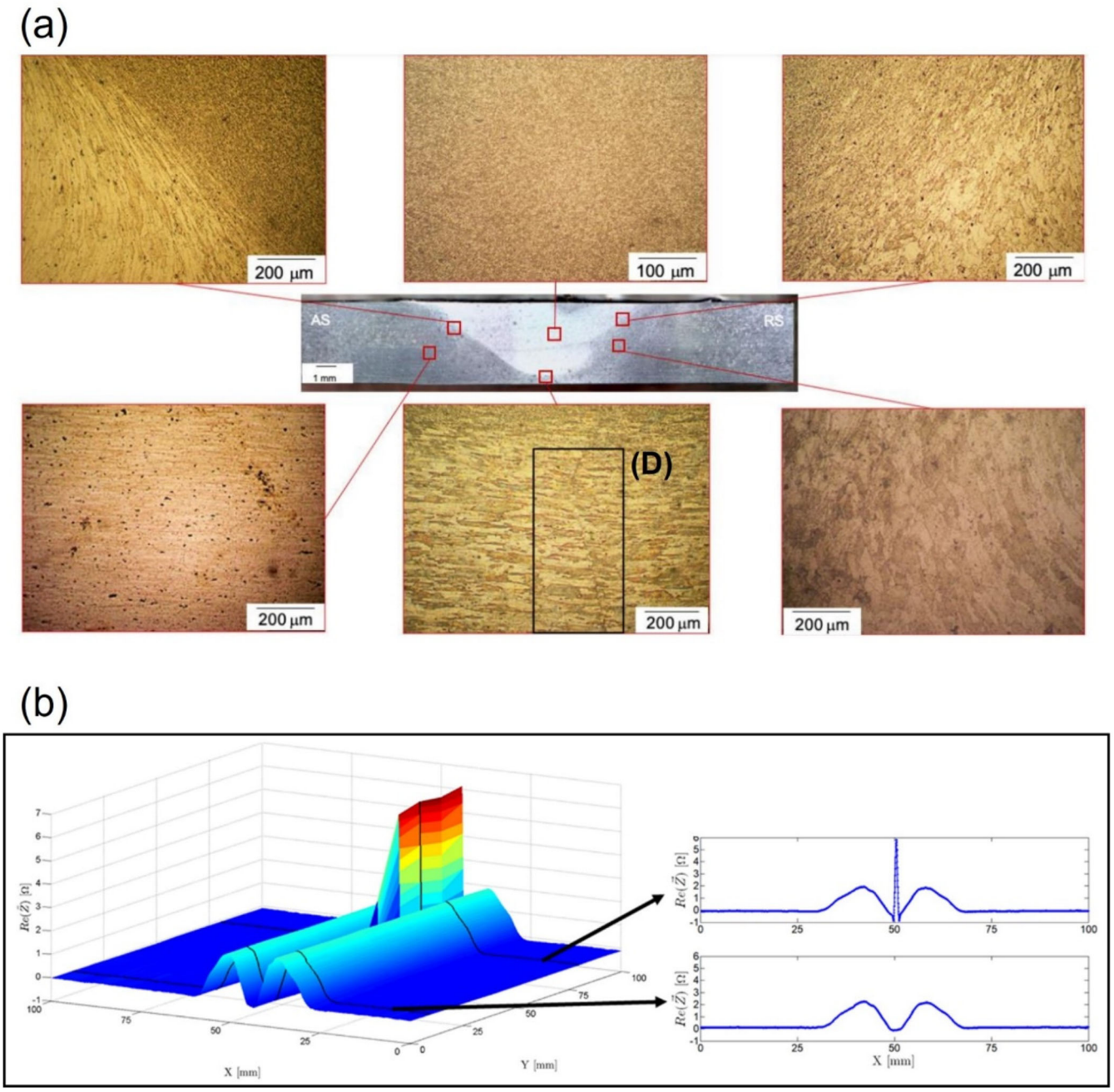

Figure 2. (a) Cross sectional micrographs of the welding region and (b) EC testing output over a defective area (D). On the left a C-scan is represented where the electric impedance is displayed for each XY position. On the right, two 2D graphs are displayed with the electric impedance change over the X length for two different Y positions, with and without defect.

2.7. Fatigue testing

Fatigue testing was carried out on an Instron servo hydraulic machine (model P8502) equipped with a load cell of 10 kN. The tests were performed at two different temperatures: room temperature (23 °C) and at 150 °C. The specimens used for these tests were in all aspects equals to the ones used in the uniaxial quasi-static tensile tests. All the fatigue tests were carried out until the fatigue specimens fractured or until the run-out limit, established at $2x10^6$ cycles, was attained. The fatigue tests were conducted under 2 stress ratios (R = 0.5 and R = 0.05) at each loading temperature.

3. Results and discussion

3.1. Characterization of the welds with and without defects

The aluminum plates welded with the parameters listed in Table 2 were subject to EC testing to assist in the selection of the appropriate process parameters. The EC testing was performed to assess the presence of root defects in the specimens. Several scans were performed over the joint, on the opposite side of where the FSW tool traveled (i.e., along the weld root), in the weld transversal direction over the course of 100 mm. Figure 2 depicts the impedance change over the

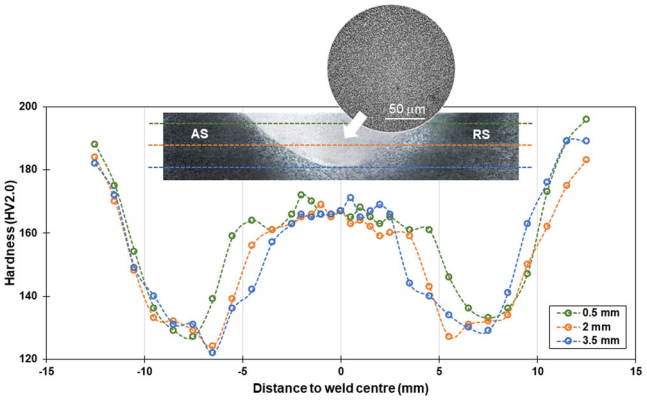

Figure 3. Hardness profiles at 0.5, 2 and 3.5 mm from the top surface of a non-defective weld (produce with the parameters presented in Table 3).

surface of one defective welded plate as an example of an EC testing performed. As observed, the output along the transversal direction toward the weld joint (X direction) depicts two humps just as it happens with the hardness profiles (Figure 3), only inverted. This is directly related to the electrical conductivity change, which is higher in HAZ and suffers a decrease in the nugget due to the grain refinement. In the second half of this welded plate, a root defect was generated, and it is represented by the localized impedance change in the nugget zone and seen in the C-scan with warmer colors. All the specimens were subject to EC testing, which allowed to reduce the parameters range that generate defect-free welds.

Furthermore, through the analysis of the macro and micrographs obtained, it was possible to clearly identify all the typical microstructural regions of welds obtained by FSW (Figure 3). The stir zone appears in the center of the macrographs in a clearer color tone (whiter). In this region, a fine, homogeneous, equiaxed microstructure can be encountered as a result of the dynamic recrystallization that the material undergoes, due to the intense plastic and frictional deformation, similarly to previously reported studies [16]. Regarding the TMAZ, it can be identified as being the closest region to the stir zone, with a slightly darker color tone and a different grain morphology. When observing the micrographs corresponding to the TMAZ, it is possible to identify the highly deformed grain structure that characterizes this region (Figure 4a). This highly deformed microstructure is more evident in the interface between the nugget and the TMAZ. Another important aspect worth mentioning is that the micrographs also clearly shows that the transition between the TMAZ and the dynamic recrystallization zone is smoother and harder to detect at the retreating side of the weld. As for the HAZ, it can be identified as being the region with a darker tone and different grain morphology comparatively to the one presented by the TMAZ. Regarding its microstructure, the grain size is higher when compared to the one found in the aforementioned regions and more strengthening precipitates are encountered (Figure 4b). Figure 4b shows the presence of precipitates which is now to be one of the strengthening processes of AA7075 aluminum alloys, leading to higher hardness and tensile strength [17, 18]. The second phase particles

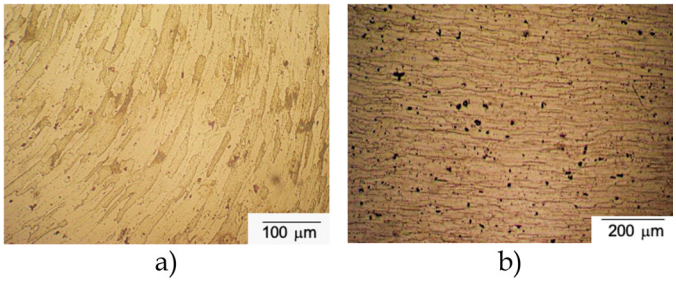

Figure 4. Optical microscopy of the a) TMAZ and b) HAZ of a welded joint produced with the parameters listed in Table 3.

observed in Figure 4b in black are smaller than 10 μm, consistent with AA7075 FSW microstructures reported in the literature [19]. These microstructural changes are consistent with the literature for AA7075 aluminum alloy, such as in [20] where a refinement in the order of ten was reported along with a decrease in the order of two of Al_7Cu_2Fe constituent particles.

Vickers hardness tests were carried out at 0.5, 2 and 3.5 mm from the upper surface of the welds. The hardness profiles obtained for the welds produced with the parameters presented in Table 3 are shown in Figure 3.

Regarding the hardness measurement results, it was possible to identify a plateau surrounding the weld center, which extents up to approximately 4 mm, on both sides, where the hardness remains approximately constant (Figure 3). This hardness uniformity is a result of the homogeneous microstructure found in the dynamic recrystallization zone (nugget), which has been discussed previously. The hardness values decrease progressively along the TMAZ (as the distance to the weld center increases) with the absolute minimum hardness values being registered, primarily, in the advancing side of the weld and more specifically, at the interface between the HAZ and the TMAZ (for both sides of the weld, the lowest hardness values are found at this interface). Similar results were obtained by Balasubramanian et al. [21].

According to Pankade et al. [22], who analyzed the hardness profile obtained for AA7075 T6 friction stir welds and obtained identical results, such an observation can be explained by the precipitate over-aging and consequent coarsening that occurs in this region, as a result of the thermal cycle that the material undergoes. Along the HAZ, the increase in distance to the weld center is accompanied by a hardness increase since, gradually, lower temperatures and cooling rates are attained as the distance to the base material decreases. From Figure 3 it is noticeable that the hardness profile is similar along the welded plate thickness, being the plateau width the most depicted difference, which is related with the nugget size and geometry, being this narrower at the bottom of the weld, near the weld root, and wider at the top of the weld.

3.2. Uniaxial quasi-static test results

Preliminary welds subject to tensile testing revealed similar mechanical strength with an average value of 367.5 MPa and a standard deviation of 12.3 MPa (Figure 5), which

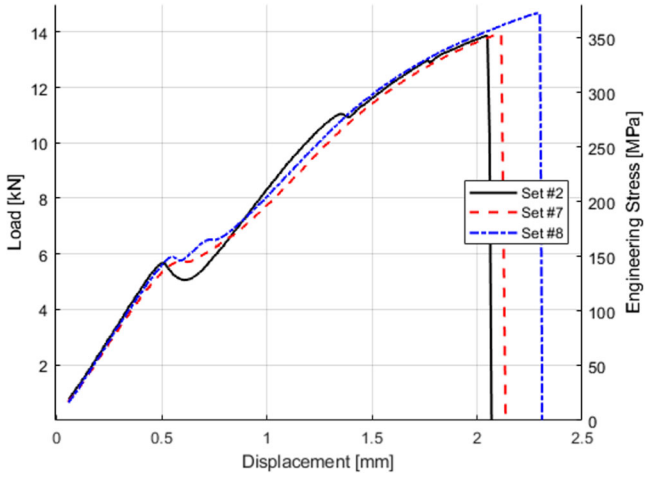

Figure 5. Load-Displacement curves for preliminary welding plates.

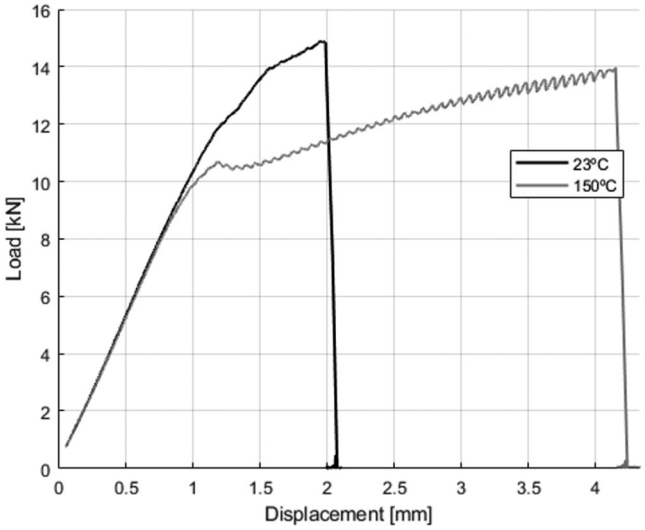

Figure 6. Load-Displacement curves obtained at room (23 °C) and elevated (150 °C) temperatures on specimens produced with the welding parameters indicated in Table 3.

corresponds to a joint efficiency of approximately 64%, when compared to the base material (572 MPa). These results are in good accordance with those reported by Balasubramanian et al. [10], Çevik et al. [23] and Linton & Ripley [24]. From Figure 5 it is also possible to observe that necking did not occur for any specimen and that they all present a very similar ductile behavior.

Based on these results, the parameters used in Set #8 were selected to produce welded specimens for fatigue testing and uniaxial quasi-static tests at 150 °C. Uniaxial quasi-static tests of welds produced with this parameter set were then used to set the fatigue testing loads. in the results of uniaxial quasi-static testing at both temperatures is presented in Figure 6. A temperature increase from ~23 °C to 150 °C did not drastically decrease the ultimate tensile strength of the welds, although it had a significant effect on ductility. At this elevated temperature, the weld's ultimate tensile strength was approximately 355 MPa, which represents a joint efficiency of approximately 62%, when compared to the base material (Table 1).

3.2.1. Tensile fracture surfaces analysis

After quasi-static tensile testing, the fracture surfaces of the specimens were analyzed. The failure location (initial location and development direction), as well as the observed type of fracture for each specimen, can be found in Table 4.

The fracture, and the corresponding propagation mechanism, of the specimen tested at room temperature started at the root of the weld and propagated in a 45° plane toward the region where the lowest hardness values were recorded (TMAZ/HAZ interface).

In what concerns to the high temperature specimens, the tensile fracture also started at the root of the weld, however, the propagation evolved perpendicularly (according to a 90° plane) to the applied stress.

This way, it can be stated that the failure mechanism common to all specimens was the fracture nucleation at the weld root, fact that can be associated to processing defects generated in the same region. These defects may have resulted from improper/insufficient material mixing during the welding process, weakening the root region, leading to the observed failure mode. Furthermore, the extension of this area may have induced the direction along which the fracture evolved.

Even tough EC nondestructive testing enables the detection of such defects, depending on defect size and resolution limitations, some root defects may pass undetected leading to the initiation of failure at this location while being marked as defect free specimens.

3.3. Fatigue test results

The results obtained through the execution of the fatigue tests at 23 °C and 150 °C are presented in the form of S-N curves, for the maximum stress applied, in Figure 7. Regarding the S-N curves obtained considering the stress range applied during the tests carried out at 23 °C and 150 °C, they can be found in Figure 8.

The fatigue life of the specimens was found to be lower when the lowest stress ratio (R = 0.05) was applied, when considering the maximum stress applied during the tests. This means that for the same number of cycles, the maximum stress needed to cause failure in R = 0.05 condition is lower comparatively to the one required for R = 0.5 conditions. Relative to the stress range, the lowest stress ratio was found to result in a higher fatigue life of the specimens. These trends were observed for both loading temperatures. Regarding the temperature effect over the fatigue life of the specimens, it is also easy to perceive the negative impact of the use of 150 °C as testing temperature: when the same stress ratio and maximum stress (or similar) were applied to the specimens at room temperature, fatigue failure occurred at a significantly higher number of cycles, comparatively to the ones obtained at 150 °C. Such a trend was expected, considering the work developed by Resan et al. [11] and Tra et al. [12].

The material was also found to be sensitive to mean stress applied, since the S-N curves obtained for the maximum stress were less spaced that the ones obtained for the stress range, for both loading temperatures.

Table 4. Tensile specimens' fracture location and correspondent type of fracture.

Test Temperature	Initial fracture location and development direction	Type of fracture
23 °C	The fracture initiates at the bottom surface of the specimen, at the root of the weld, and posteriorly evolves toward the HAZ	Ductile with the fracture occurring at 45° relatively to the applied stress
150 °C	The fracture initiates at the bottom surface of the specimen, at the root of the weld, and then evolved toward its center, through the middle of the weld	Ductile with the fracture occurring perpendicularly to the applied stress

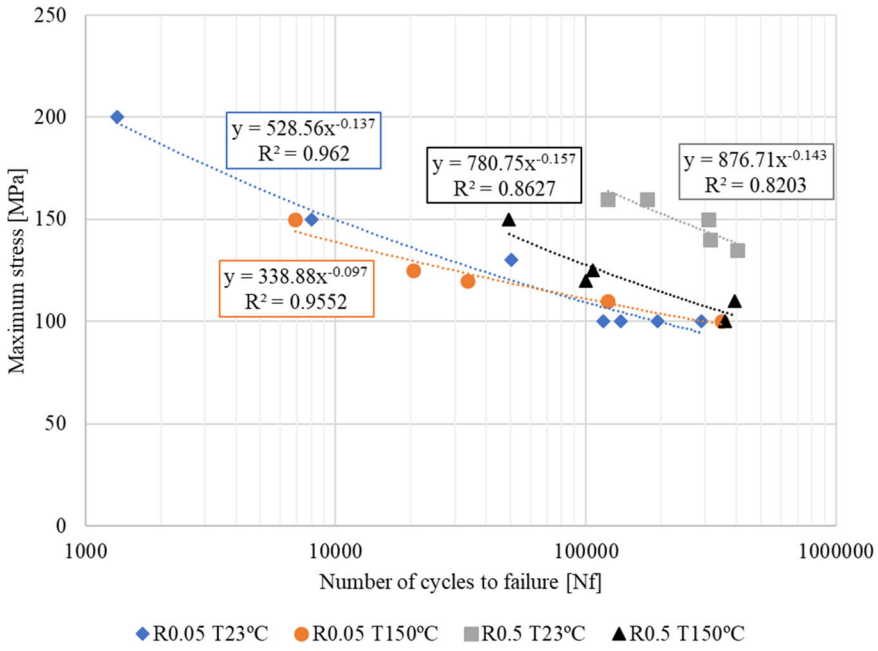

Figure 7. S-N curves obtained for the fatigue tests carried out at R = 0.05 and R = 0.5, at room temperature (23 °C) and at high temperature (150 °C), considering the maximum stress applied during the fatigue tests.

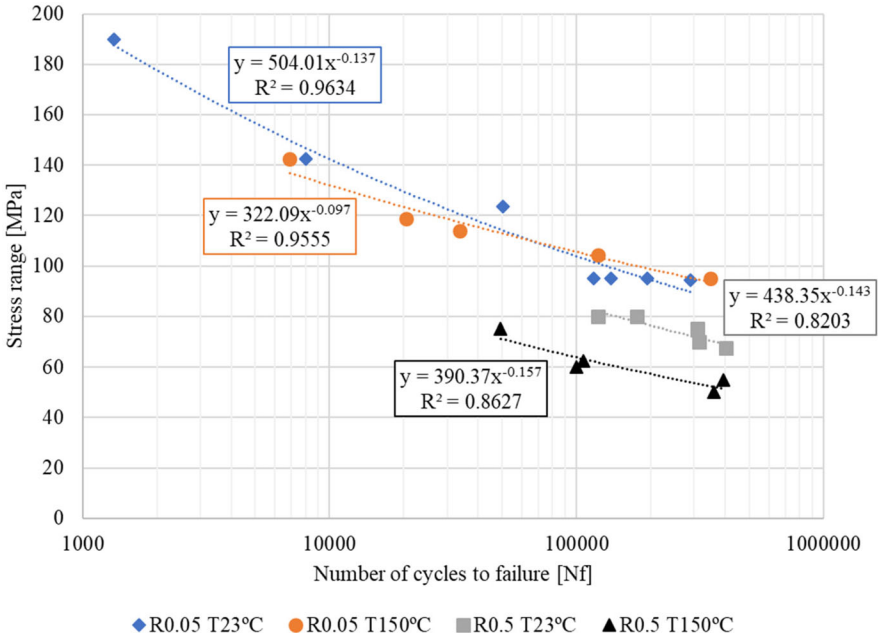

Figure 8. S-N curves obtained for the fatigue tests carried out at R = 0.05 and R = 0.5, at room temperature (23 °C) and at high temperature (150 °C), considering the stress range applied during the fatigue tests.

3.3.1. Fatigue fracture surfaces analysis

A visual analysis was conducted on the specimens that underwent fatigue testing and for which fracture occurred. This analysis was performed with the purpose of identifying the location, within the weld, where the fatigue crack nucleated, the type of fatigue crack present in each specimen and the direction along which the propagation process took place. This information is summarized in Table 5.

Table 5. Properties of the fatigue fracture surfaces obtained for the fatigue specimens.

Test Temperature	Fatigue fracture surfaces properties
23 °C	• Fracture occurred according to a 45° plane, relatively to the applied stress. Through type of crack with the nucleation process starting at the bottom surface of the specimen, at the root of the weld • Fracture occurred according to a 45° and to 90° plane, relatively to the applied stress. Semi-elliptical type of crack that nucleated at the bottom surface of the specimen, at the root of the weld • Fracture occurred according to a 90° plane, relatively to the applied stress. Corner type of crack that nucleated at the bottom surface of the specimen, at the root of the weld. The crack propagated to near the top surface of the weld • In a few specimens secondary cracking was observed
150 °C	• Fracture occurred according to a 90° plane, relatively to the applied stress. Semi-elliptical type of crack that nucleated at the bottom surface of the specimen, at the root of the weld. The crack then propagated to near the top surface of the weld

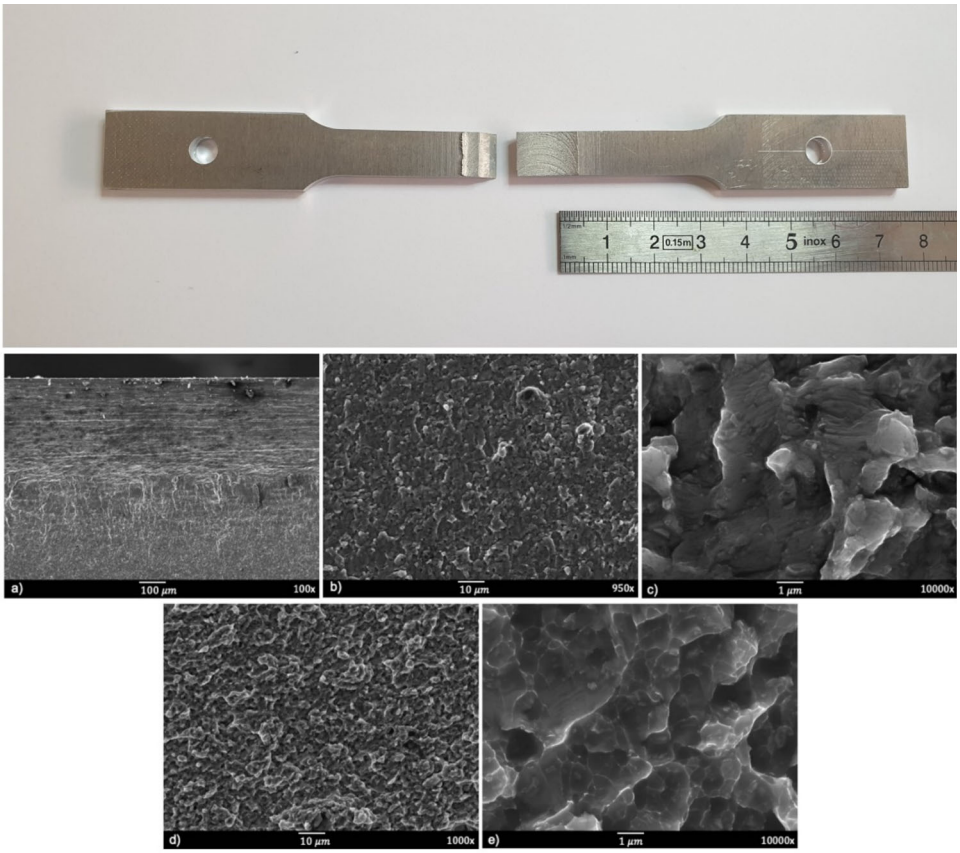

Figure 9. Fractographies of a specimen tested with R = 0.5 and T = 23 °C: a) crack initiation region, b) crack propagation region, c) fatigue striations, d) final fracture region with visible dimples, e) detail of d).

Considering the number of specimens tested, this analysis is intended to be a representative one.

3.3.2. Fatigue fracture surfaces characterization by scanning electron microscopy

Two fatigue specimens were selected to be observed using a Scanning Electron Microscope, SEM, with the purpose of identifying in more detail the morphology of the fatigue crack nucleation and propagation mechanism. The results obtained are shown in Figures 9 and 10.

From the results obtained by the analysis that was performed over the fatigue fracture surfaces, it is possible to see that the fatigue process took place in three distinct regions, with each region resulting from a different fatigue stage: i) crack initiation region, ii) crack propagation region, illustrated by the presence of fatigue striations and iii) final fracture region, illustrated by the presence of dimples.

Crack initiation occurs, for all specimens, at the root of the weld. According to the work developed by other authors, in friction stir welds that are free of defects, the crack initiation process usually starts off at the top surface of the weld, from surface irregularities that could be a result of marks left by the FSW tool [25, 26]. Since, according to the nondestructive tests that were carried out, no welding defects were detected in the welds from which the fatigue specimens were manufactured from, a weaker zone at the root of the weld, that could have resulted from an improper/insufficient material mixing, could be the reason behind such an observation. Although the fatigue crack nucleated at the root of the weld in all specimens, its propagation was found to occur along two possible directions (for

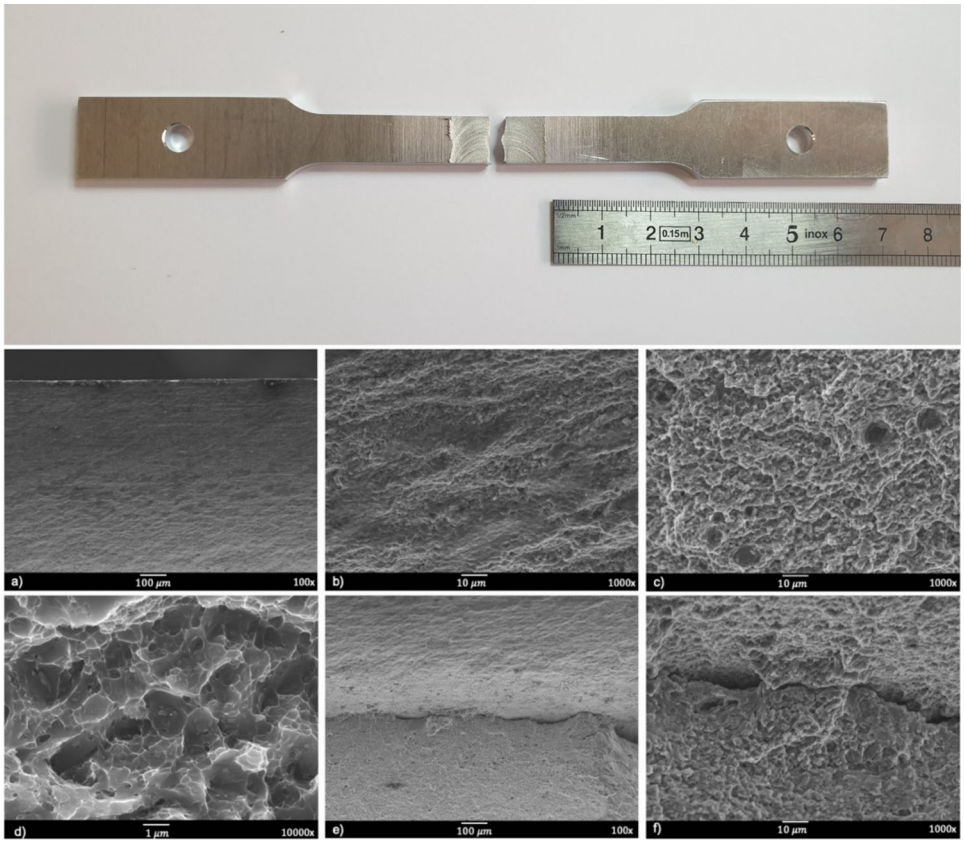

Figure 10. Fractographies of a specimen tested with R = 0.05 and T = 23 °C: a) crack initiation region, b) final fracture region, c) final fracture regions showing dimples, d) detail of c), e) secondary cracking, f) detail of e).

the specimens tested at room temperature): according to a 45° or 90° plane, relatively to the applied stress. The latter was expected [27] and an effort was made in order to correlate the direction of the crack propagation and the stress range used during the fatigue tests.

Analyzing the fatigue results presented in Figures 7 and 8, it is possible to conclude that, generally, lower stress ranges resulted in the fatigue crack propagating at 45°, which can be a result of the machine's lower clamp rotation combined with a possible misalignment of the fatigue specimens. All specimens tested at high temperature fractured according to a 90° plane, relatively to the applied stress.

The crack propagation process takes place after the crack attains a certain dimension (usually in the order of some grains size). The region through which the crack propagates was easily identified while analyzing the surfaces' fractographies, due to the presence of its most characteristic feature: striations. Fatigue striations are a result of the crack tip deformation during a complete load cycle. In fact, each striation results from a load cycle and marks the successive position of the front of the crack in the moment that the striation was formed. The spacing between each one corresponds to the crack growth during each load cycle. Striations are usually aligned perpendicularly to the crack propagation direction and invariably bowed toward that direction as well, since their growth is facilitated closer to the crack tip comparatively to the borders, where their growth is restrained (for example by grain boundaries). The crack initiation and propagation regions combine to make up a smooth region in the fracture surface that has a silky and shiny appearance. Such an appearance is a result of the rubbing of the crack surfaces during its propagation process. As for the final region of the fracture surfaces, where the final fracture took place, it is characterized by a darker region with a more coarse and irregular appearance. This final fracture takes place when that region, the remaining cross-sectional area of the specimen, is not capable of withstanding the stress that is being applied. In this region, the mechanisms that led to the crack propagation are progressively replaced by static fracture mechanisms. In this stage of the fatigue process, the crack growth rate increases exponentially, and the specimen's fracture becomes unpredictable. As a result of both the microstructure of the specimens and the alternated stress applied to them during fatigue testing, a final ductile fracture is obtained. Such a type of fracture is revealed by the existence of small voids, depressions - dimples - that are easily depicted through the analysis of the fractographies obtained by the SEM.

4. Conclusions

The main conclusions that arose from the present work are the following:

- Both samples presented a W-shaped hardness profile which is characteristic of friction stir welds of heat treatable aluminum alloys.

- Regarding the UTS, similar values were obtained for the specimens that underwent uniaxial quasi-static tensile tests, with an average of 367.5 MPa (standard deviation of 12.3 MPa), which corresponds to a joint efficiency of 64%.
- The fatigue life of the AA7075-T651 friction stir welds was found be lower when the lowest stress ratio was applied: R = 0.05, considering the maximum stress applied, at both loading temperatures. The contrary was also found to be true, for the stress range applied.
- The fatigue life of the specimens at the higher loading temperature was significantly lower when compared to fatigue tests conducted at a similar stress range, with the same stress ratio, at room temperature (23 °C).

Funding

This work was supported by FCT, through IDMEC under LAETA, project UIDB/50022/2020. MAM and CV acknowledge Fundação para a Ciência e a Tecnologia (FCT MCTES) for its financial support via the project UIDB/00667/2020 (UNIDEMI).

ORCID

Daniel F. O. Braga http://orcid.org/0000-0002-0587-3041
Catarina Vidal http://orcid.org/0000-0002-7622-847X
Virgínia Infante http://orcid.org/0000-0003-0860-2404

References

[1] A.N. Correia, D.F.O. Braga, P.M.G.P. Moreira, and V. Infante, Review on dissimilar structures joints failure, Eng. Fail. Anal., vol. 129, p. 105652, 2021. DOI: 10.1016/j.engfailanal.2021.105652.
[2] V. Patel, W. Li, G. Wang, F. Wang, A. Vairis, and P. Niu, Friction stir welding of dissimilar aluminum alloy combinations: state-of-the-art, Metals (Basel), vol. 9, no. 3, pp. 270, 2019. DOI: 10.3390/met9030270.
[3] V. Patel, et al., High-speed friction stir welding in light weight battery trays for the EV industry, Sci. Technol. Weld. Join., vol. 27, no. 4, pp. 250–255, 2022. DOI: 10.1080/13621718.2022.2045121.
[4] V. Patel, et al., High speed friction stir welding of AA6063-T6 alloy in lightweight battery trays for EV industry: influence of tool rotation speeds, Mater. Lett., vol. 318, pp. 132135, 2022. DOI: 10.1016/j.matlet.2022.132135.
[5] D. Sejani, W. Li, and V. Patel, Stationary shoulder friction stir welding – low heat input joining technique: a review in comparison with conventional FSW and bobbin tool FSW, Crit. Rev. Solid State Mater. Sci., pp. 1–50, 2021. DOI: 10.1080/10408436.2021.1935724.
[6] X. Meng, Y. Huang, J. Cao, J. Shen, and J.F. dos Santos, Recent progress on control strategies for inherent issues in friction stir welding, Prog. Mater. Sci., vol. 115, pp. 100706, 2021. DOI: 10.1016/j.pmatsci.2020.100706.
[7] L.S. Rosado, T.G. Santos, M. Piedade, P.M. Ramos, and P. Vilaça, Advanced technique for non-destructive testing of friction stir welding of metals, Measurement., vol. 43, no. 8, pp. 1021–1030, 2010. DOI: 10.1016/j.measurement.2010.02.006.
[8] T.G. Santos, P. Vilaça, and R.M. Miranda, Electrical conductivity field analysis for evaluation of FSW joints in AA6013 and AA7075 alloys, J. Mater. Process. Technol., vol. 211, no. 2, pp. 174–180, 2011. DOI: 10.1016/j.jmatprotec.2010.08.030.
[9] V. Patel, W. Li, X. Liu, Q. Wen, and Y. Su, Through-thickness microstructure and mechanical properties in stationary shoulder friction stir processed AA7075, Mater. Sci. Technol., vol. 35, no. 14, pp. 1762–1769, 2019. DOI: 10.1080/02670836.2019.1641459.
[10] G. Sun, X. Wei, D. Shang, S. Chen, L. Long, and X. Han, Tensile and fatigue analysis based on microstructure and strain distribution for 7075 aluminum FSW joints, Metals (Basel), vol. 10, no. 12, pp. 1610, 2020. DOI: 10.3390/met10121610.
[11] Kadhim, K. Resan, A.A. Alassadi, M.Al-Waily, and M.J. Jweeg, Influence of temperature on fatigue life for friction stir welding of aluminum alloy materials, Int. J. Mech. Mechatron. Eng., vol. 18, no. 2, pp. 1–9, 2018.
[12] T.H. Tra, M. Okazaki, and K. Suzuki, Fatigue crack propagation behavior in friction stir welding of AA6063-T5: Roles of residual stress and microstructure, Int. J. Fatigue, vol. 43, pp. 23–29, 2012. DOI: 10.1016/j.ijfatigue.2012.02.003.
[13] S. Li, Aluminum Friction Stir Welding Head Fatigue Crack Growth Rate Pilot Study, Lanzhou University of Technology, Lanzhou, China, 2008.
[14] J.R. Davis, ASM Specialty Handbook: Aluminum and Aluminum Alloys, ASM International, OH, USA, 1993.
[15] V.R. Duarte, et al., Benchmarking of nondestructive testing for additive manufacturing, 3D Print Addit Manuf., vol. 8, no. 4, pp. 263–270, 2021. DOI: 10.1089/3dp.2020.0204.
[16] V. Patel, W. Li, A. Vairis, and V. Badheka, Recent development in friction stir processing as a solid-state grain refinement technique: microstructural evolution and property enhancement, Crit. Rev. Solid State Mater. Sci., vol. 44, no. 5, pp. 378–426, 2019. DOI: 10.1080/10408436.2018.1490251.
[17] V. Patel, V. Badheka, W. Li, and S. Akkireddy, Hybrid friction stir processing with active cooling approach to enhance superplastic behavior of AA7075 aluminum alloy, Arch. Civ. Mech. Eng., vol. 19, no. 4, pp. 1368–1380, 2019. DOI: 10.1016/j.acme.2019.08.007.
[18] V. Patel, et al., Tailoring grain refinement through thickness in magnesium alloy via stationary shoulder friction stir processing and copper backing plate, Mater. Sci. Eng.: A, vol. 784, pp. 139322, 2020. DOI: 10.1016/j.msea.2020.139322.
[19] M. Navaser, and M. Atapour, Effect of friction stir processing on pitting corrosion and intergranular attack of 7075 aluminum alloy, J. Mater. Sci. Technol., vol. 33, no. 2, pp. 155–165, 2017. DOI: 10.1016/j.jmst.2016.07.008.
[20] J.J. Pang, F.C. Liu, J. Liu, M.J. Tan, and D.J. Blackwood, Friction stir processing of aluminium alloy AA7075: Microstructure, surface chemistry and corrosion resistance, Corros. Sci., vol. 106, pp. 217–228, 2016. DOI: 10.1016/j.corsci.2016.02.006.
[21] P. Sivaraj, D. Kanagarajan, and V. Balasubramanian, Effect of post weld heat treatment on tensile properties and microstructure characteristics of friction stir welded armour grade AA7075-T651 aluminium alloy, Defence Technol., vol. 10, no. 1, pp. 1–8, 2014. DOI: 10.1016/j.dt.2014.01.004.
[22] S.B. Pankade, P.M. Ambad, R. Wahane, and C.L. Gogte, Effect of the post-weld heat treatments on mechanical and corrosion properties of friction Stir-Welded AA 7075-T6 aluminium alloy, in Strengthening and Joining by Plastic Deformation, Uday Shanker Dixit, R. Ganesh Narayanan (eds.), Springer, Singapore, 2019, pp. 79–94.
[23] B. Çevik, Y. Özçatalbaş, and B. Gülenç, Friction Stir Welding of 7075-T651 aluminium alloy, Pract. Met., vol. 53, no. 1, pp. 6–23, 2022. DOI: 10.3139/147.110363.
[24] V.M. Linton, and M.I. Ripley, Influence of time on residual stresses in friction stir welds in age hardenable 7xxx aluminium alloys, Acta Mater., vol. 56, no. 16, pp. 4319–4327, 2008. DOI: 10.1016/j.actamat.2008.04.059.
[25] G. Pouget, and A.P. Reynolds, Residual stress and microstructure effects on fatigue crack growth in AA2050 friction stir welds, Int. J. Fatigue, vol. 30, no. 3, pp. 463–472, 2008. DOI: 10.1016/j.ijfatigue.2007.04.016.
[26] H. Li, J. Gao, and Q. Li, Fatigue of friction stir welded aluminum alloy joints: a review, Appl. Sci., vol. 8, no. 12, pp. 2626, 2018. DOI: 10.3390/app8122626.
[27] Shigley, Shigley's Mechanical Engineering Design, 9th ed. McGraw-Hill, New York, 2010.